ADVANCED FUNCTIONAL MATERIALS

www.afm-journal.de

Check for updates

Mechanically Guided Post-Assembly of 3D Electronic Systems

Bong Hoon Kim, Fei Liu, Yongjoon Yu, Hokyung Jang, Zhaoqian Xie, Kan Li, Jungyup Lee, Ji Yoon Jeong, Arin Ryu, Yechan Lee, Do Hoon Kim, Xueju Wang, KunHyuck Lee, Jong Yoon Lee, Sang Min Won, Nuri Oh, Jeonghyun Kim, Ju Young Kim, Seong-Jun Jeong, Kyung-In Jang, Seungmin Lee, Yonggang Huang, Yihui Zhang,* and John A. Rogers**

This paper describes deterministic assembly processes for transforming conventional, planar devices based on flexible printed circuit board (FPCB) platforms into those with 3D architectures in a manner that is fully compatible with off-the-shelf packaged or unpackaged component parts. The strategy involves mechanically guided geometry transformation by out-of-plane buckling motions that follow from controlled forces imposed at precise locations across the FPCB substrate by a prestretched elastomer platform. The geometries and positions of cuts, slits, and openings defined into the FPCB provide additional design parameters to control the final 3D layouts. The mechanical tunability of the resulting 3D FPCB platforms, afforded by elastic deformations of the substrate, allows these electronic systems to operate in an adaptable manner, as demonstrated in simple examples of an optoelectronic sensor that offers adjustable detecting angle/area and a near-field communication antenna that can be tuned to accommodate changes in the electromagnetic properties of its surroundings. These approaches to 3D FPCB technologies create immediate opportunities for designs in multifunctional systems that leverage state-of-the-art components.

1. Introduction

Extending microsystems technologies from their conventional, 2D, multilayered layouts into forms that adopt fully 3D designs represents a promising avenue for realizing improved or differentiated functionality.[1–10] Current research in this area focuses on various methods for 3D manufacturing/assembly and their use with heterogeneous collections of advanced materials.[11–15] The ancient Japanese arts of origami and kirigami serve as design inspiration for several promising alternative approaches, but automated processes of cutting and folding that apply to a full range of functional thin film materials and across length scales, from micrometer to centimeter dimensions, do not currently exist.[16–21] Some of the most attractive techniques rely on 2D to 3D geometrical transformation by action of forces

Dr. B. H. Kim, Dr. X. Wang, K. H. Lee
Department of Materials Science and Engineering
Simpson Querrey Institute and Feinberg Medical School
Center for Bio-Integrated Electronics
Northwestern University
Evanston, IL 60208, USA

F. Liu, Prof. Y. Zhang
Center for Mechanics and Materials
Center for Flexible Electronics Technology
AML, Department of Engineering Mechanics
Tsinghua University
Beijing 100084, China
E-mail: yihuizhang@tsinghua.edu.cn

Y. Yu, H. Jang, J. Lee, J. Y. Jeong, A. Ryu, Y. Lee, D. H. Kim, J. Y. Lee, S. M. Won
Frederick Seitz Materials Research Laboratory
University of Illinois at Urbana-Champaign
Urbana, IL 61801, USA

Dr. Z. Xie, K. Li
Department of Civil and Environmental Engineering
Mechanical Engineering, and Materials Science and Engineering
Northwestern University
Evanston, IL 60208, USA

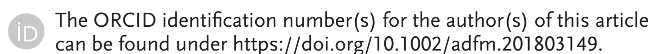
The ORCID identification number(s) for the author(s) of this article can be found under https://doi.org/10.1002/adfm.201803149.

DOI: 10.1002/adfm.201803149

Dr. Z. Xie, K. Li
AML, Department of Engineering Mechanics
Center for Mechanics and Materials
Tsinghua University
Beijing 100084, China

Prof. N. Oh
Division of Materials Science and Engineering
Hanyang University
Seoul 04763, Republic of Korea

Prof. J. Kim
Department of Electronics Convergence Engineering
Kwangwoon University
Seoul 01897, Republic of Korea

Dr. J. Y. Kim
Multidisciplinary Sensor Research Group
Electronics and Telecommunications Research Institute (ETRI)
Daejeon 34129, Republic of Korea

Prof. S.-J. Jeong
Department of Organic Materials and Fiber Engineering
Department of Information Communication
Materials, and Chemistry Convergence Technology
Soongsil University
369 Sangdo-ro, Dongjak-gu, Seoul 06978, Republic of Korea

Prof. K.-I. Jang
Department of Robotics Engineering
Daegu Gyeongbuk Institute of Science and Technology (DGIST)
Daegu 42988, Republic of Korea

© 2018 WILEY-VCH Verlag GmbH & Co. KGaA, Weinheim

derived from mismatch strains,[22–24] capillary effects,[25] electromagnetic interactions,[26] or dimensional change.[27] A variety of simple 3D layouts can be achieved in this way, although with important limitations in speeds of assembly, levels of engineering control, options in constituent materials, and ranges of accessible device types. A recent collection of methodologies based on mechanically guided assembly use, instead, prestrain in an elastomeric substrate to affect transformation of prefabricated 2D constructs into 3D architectures, in a manner that bypasses many constraints of other approaches and offers full compatibility with the most successful 2D microsystems and manufacturing processes.[28–31]

This paper highlights the application of these core ideas to flexible printed circuit board (FPCB) technologies to yield 3D functional constructs with various embedded and interconnected semiconductor device components in a broad span of geometries. An appeal of the traditional 2D FPCB platform is that it is exceptionally well developed as a low-cost, widely commercialized vehicle capable of addressing diverse applications in electronic and optoelectronic systems by virtue of lightweight, space efficient attributes, and its backward compatibility with PCB manufacturing.[32,33] The following introduces some simple procedures for spontaneously transforming complete, functional FPCB platforms into 3D architectures. The process uses strategically designed openings and cuts across the FPCB platform for mechanically guided assembly by controlled buckling.[34]

Here, a prestrained silicone elastomer substrate serves as an assembly platform via its ability to impose, simultaneously and across large areas, engineered distributions of forces required to affect geometric transformation.[35] Mechanics modeling determines how the prestrain, the layouts of cuts and openings in the FPBC, and the locations of its bonding to the silicone determine the final 3D configurations. With experimentally validated computational tools for guidance, a diverse range of 3D electrical circuit shapes can be achieved.[36] Specifically, this form of kirigami provides a route to 3D FPCB systems that not only retains the benefits of conventional 2D FPCB platforms, but also affords the ability to stretch with linear elastic response to large strain deformations. The resulting 3D shapes create design opportunities in optoelectronics/photovoltaics where the detection area/angle can be defined in unique ways, in radio frequency devices where electromagnetic coupling can be controlled through geometry, and in reconfigurable systems, where the elastic stretchability affords a reversible tuning mechanism. Representative devices described in the following demonstrate these possibilities.

Prof. S. Lee
Department of Energy Electronics Convergence
Kookmin University
Seoul 02707, Republic of Korea
Prof. Y. Huang
Department of Civil and Environmental Engineering
Mechanical Engineering
Materials Science and Engineering
Northwestern University
Evanston, IL 60208, USA
E-mail: y-huang@northwestern.edu
Prof. J. A. Rogers
Department of Materials Science and Engineering
Department of Biomedical Engineering
Department of Chemistry
Department of Neurological Surgery
Department of Mechanical Engineering
Department of Electrical Engineering and Computer Science
Simpson Querrey Institute and Feinberg Medical School
Center for Bio-Integrated Electronics
Northwestern University
Evanston, IL 60208, USA
E-mail: jrogers@northwestern.edu

2. Results and Discussion

The illustration in **Figure 1**a outlines a progression in printed circuit board technology, beginning with 2D PCBs in rigid and then flexible forms, followed by the next logical step in 3D, stretchable PCBs introduced here. Figure 1b summarizes the process. The examples described in the following use bilayer FPCBs that consist of copper (thickness ≈ 9 µm) traces and polyimide (thickness ≈ 12 µm) substrates with various device components (e.g., microcontrollers, resistors, capacitors, LEDs, etc.) integrated by flip-chip or wire bonding, all according to conventional processes. Laser cutting introduces slits and openings through the polyimide in strategic locations to facilitate geometry transformation. Evaporation of Ti/SiO_2 (3/30 nm) through a shadow mask onto the back sides of such platforms defines locations of adhesion to a prestrained, silicone elastomer substrate.[37] Releasing the prestrain forms the final 3D FPCB system. The geometry of the 2D FPCB, including the slits and openings, along with the configuration of bonding sites and magnitude of the prestrain define the 3D shapes in a deterministic and predictive manner. Figure 1c,d presents photographic images and results of mechanical simulation for a FPCB in its 2D and corresponding 3D forms. Modeling by finite element analysis (FEA; see the Experimental Section for details) captures all of the essential effects, thereby providing a predictive design tool.[38–44]

The 3D FPCB demonstration system in Figure 1 involves a microcontroller, two red LEDs that switch on and off accordingly at desired frequencies and duty cycles, and two infrared (IR) LEDs that serve as photodetectors (PDs).[45] The microcontroller (RF430FRL152, Texas Instrument) supports an ISO 15693 and near-field communication (NFC, 13.56 MHz band) data exchange format (NDEF) (Figure S1, Supporting Information). Wireless communication between the device and an external controller (FEIG Electronic INC, ISO15693 long-range reader module, standard) occurs through magnetic inductive coupling. The two red LEDs (Kingbright INC, 625 nm LED) connect to general purpose input/output (GP I/O) for control; the two photodetectors (Kingbright INC, IR 940 nm LED) connect to two analog-digital converters (ADCs) for sensing. The ADCs consist of a sigma-delta modulator followed by a DC decimation filter enabling high-resolution analog-to-digital conversion of the data received. The microcontroller can be programmed using over-the-air (OVA) protocols. Commands for enabling or disabling the GP I/O or for receiving data from the ADC reside in the ferroelectric random access memory (FRAM) as program codes and measurement data. Such information can be transmitted to the long-range reader module via NDEF messages

© 2018 WILEY-VCH Verlag GmbH & Co. KGaA, Weinheim

16163028, 2018, 48, Downloaded from https://onlinelibrary.wiley.com/doi/10.1002/adfm.201803149 by Sungkyunkwan University, Wiley Online Library on [14/04/2024]. See the Terms and Conditions (https://onlinelibrary.wiley.com/terms-and-conditions) on Wiley Online Library for rules of use; OA articles are governed by the applicable Creative Commons License

16163028, 2018, 48, Downloaded from https://onlinelibrary.wiley.com/doi/10.1002/adfm.201803149 by Sungkyunkwan University, Wiley Online Library on [14/04/2024]. See the Terms and Conditions (https://onlinelibrary.wiley.com/terms-and-conditions) on Wiley Online Library for rules of use; OA articles are governed by the applicable Creative Commons License

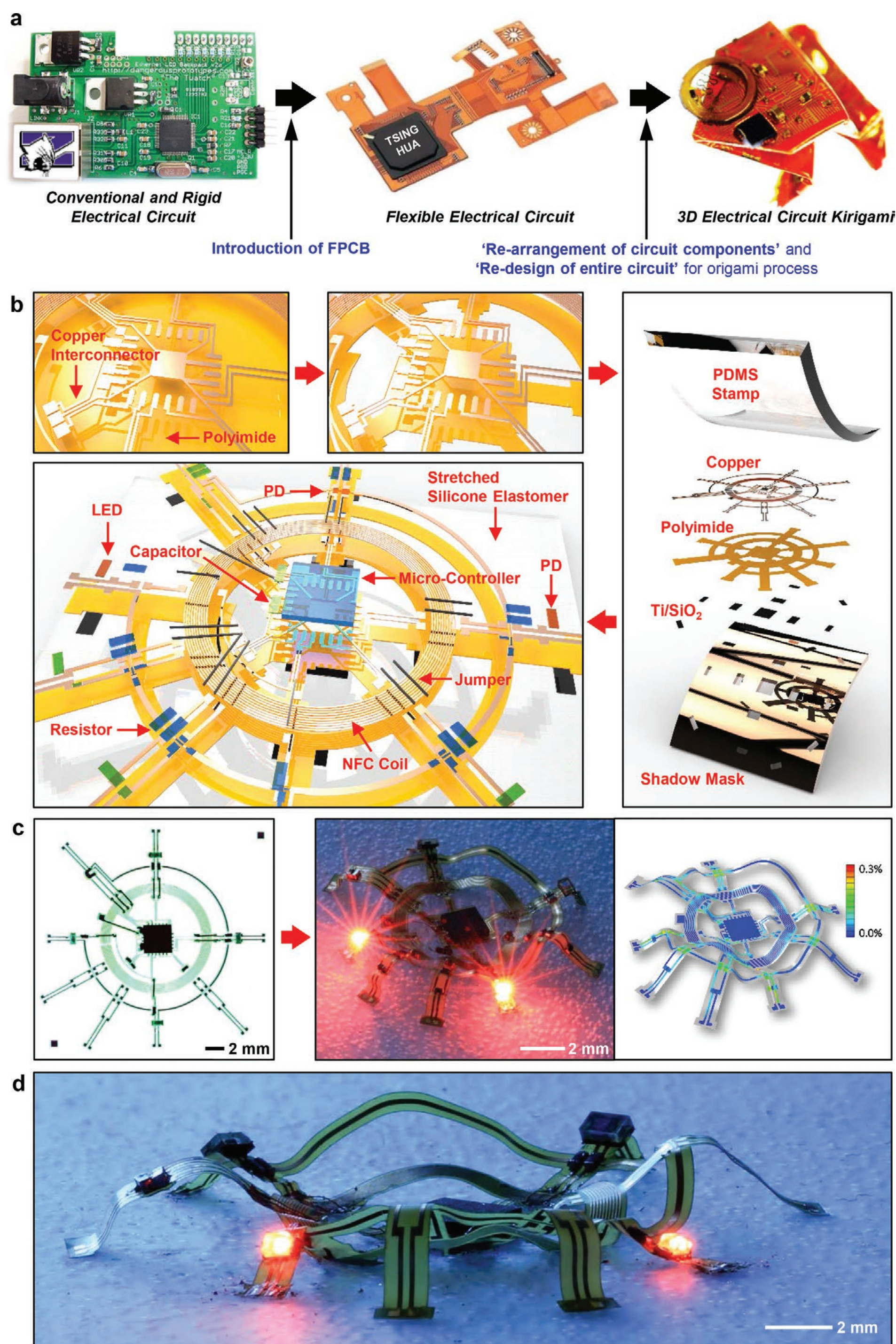

Figure 1. Materials and procedures for assembly of 3D electronic/optoelectronic systems starting from conventional 2D flexible printed circuit board (FPCB) technology. a) Concept and b) schematic illustration for the fabrication of a 3D wireless, near-field communication (NFC) platform. The 2D precursor results from conventional microfabrication and laser cutting processes applied to a standard piece of FPCB. Retrieving the circuit onto a soft stamp allows deposition of Ti/SiO_2 through a metal shadow mask onto defines bonding sites on the exposed backside surface. Transfer printing delivered the 2D precursor onto a prestretched elastomer substrate. Releasing the prestretch initiates controlled buckling processes that lead to formation of an engineered 3D structure. c,d) Photographs of the 2D precursor (left part), the 3D architecture (middle and lower part), and corresponding mechanical simulation results (right part).

(Figure S2, Supporting Information). When exposed to radio waves (high frequency, HF, 13.56 MHz) the antenna coil harvests energy, and the microcontroller distributes this power to the GP I/O pins and to the LEDs through the rectified voltage (V_{ddh}; 2.1 V) pin when the GP I/O is pulled down (LOW, 0 V). NDEF messages control the frequency and duty cycle of the

© 2018 WILEY-VCH Verlag GmbH & Co. KGaA, Weinheim

16163028, 2018, 48, Downloaded from https://onlinelibrary.wiley.com/doi/10.1002/adfm.201803149 by Sungkyunkwan University, Wiley Online Library on [14/04/2024]. See the Terms and Conditions (https://onlinelibrary.wiley.com/terms-and-conditions) on Wiley Online Library for rules of use; OA articles are governed by the applicable Creative Commons License

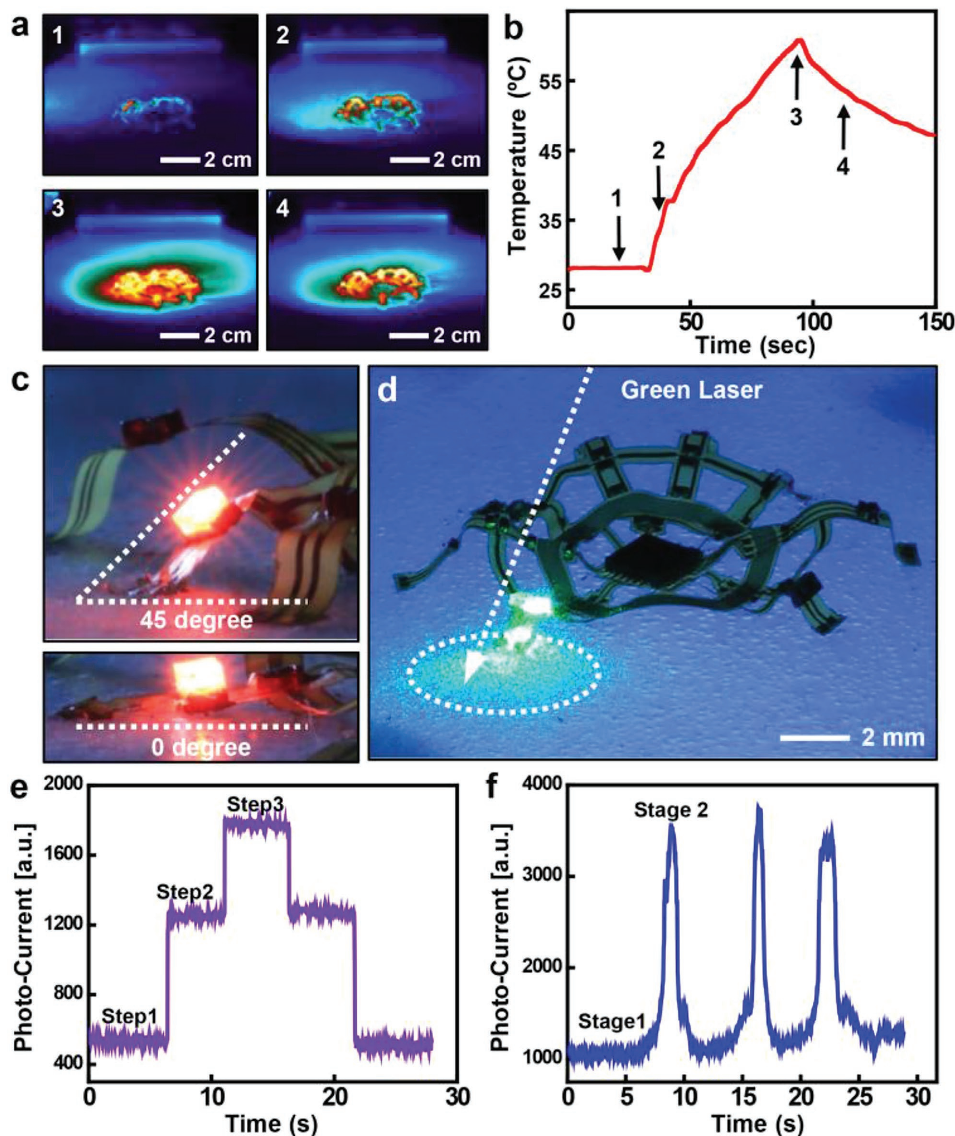

Figure 2. Functional demonstrations of a device based on a wireless, 3D FPCB system with commercial integrated components, including mechanical movements controlled by strain in the underlying elastomer substrate. a,b) Measurements of temperature induced with an external heating source placed at various distances. c) Angle between the red LED and substrate before and after 3D assembly (0° and 45°, respectively). Here, the initial prestrain in the elastomer substrate was 50% biaxial. d) Image of light from a green laser incident at a 45° angle to the photodetector. e) Plot of photocurrent in the dark (step 1), while exposed to ceiling lighting (step 2), while exposed to both ceiling lighting and flash lighting (step 3). f) Photocurrent under room lighting before 3D transformation (stage 1) and after transformation (stage 2) while a green laser is incident at a 45° angle on the photodetector as the silicon elastomer is repeatedly stretched and released.

LEDs (Figure S3, Supporting Information). A reverse bias applied to two IR LEDs allows their operation as PDs. The magnitude of photocurrents produced by these PDs transmits wirelessly as NDEF messages to the reader. In addition to optical measurements, the system can perform temperature sensing with enabled operation of a different ADC pin.

Figure 2a,b presents IR thermal images during delivery of heat with a heat gun placed at various distances, along with corresponding graphs of temperature measured wirelessly by exploiting the heat coefficient (35.7 LSB/K where LSB is the least significant bit) of the ADC. As in Figure 2c,d, the tunability of the 3D shape allows the system to operate as an optoelectronic sensor with an adjustable detecting angle/area. Specifically, as a result of stretching and releasing the silicone substrate, the positions of the red LEDs and IR PDs change in a corresponding manner. Consequently, the tilt angle of these components changes from 0° to ≈45° due to biaxial stretching to ≈50%. The operation of one of the PDs when illuminated appears in Figure 2d. Before transformation into the 3D shape, illumination with a green laser at an angle of 45° misses the PD. Releasing the prestrain causes the PD to move vertically until it intercepts the green laser. Graphs of the response of the PD for this simple demonstration and other examples of operation are in Figure 2e,f. Figure 2e shows results for operation (i) in the

 © 2018 WILEY-VCH Verlag GmbH & Co. KGaA, Weinheim

16163028, 2018, 48, Downloaded from https://onlinelibrary.wiley.com/doi/10.1002/adfm.201803149 by Sungkyunkwan University, Wiley Online Library on [14/04/2024]. See the Terms and Conditions (https://onlinelibrary.wiley.com/terms-and-conditions) on Wiley Online Library for rules of use; OA articles are governed by the applicable Creative Commons License

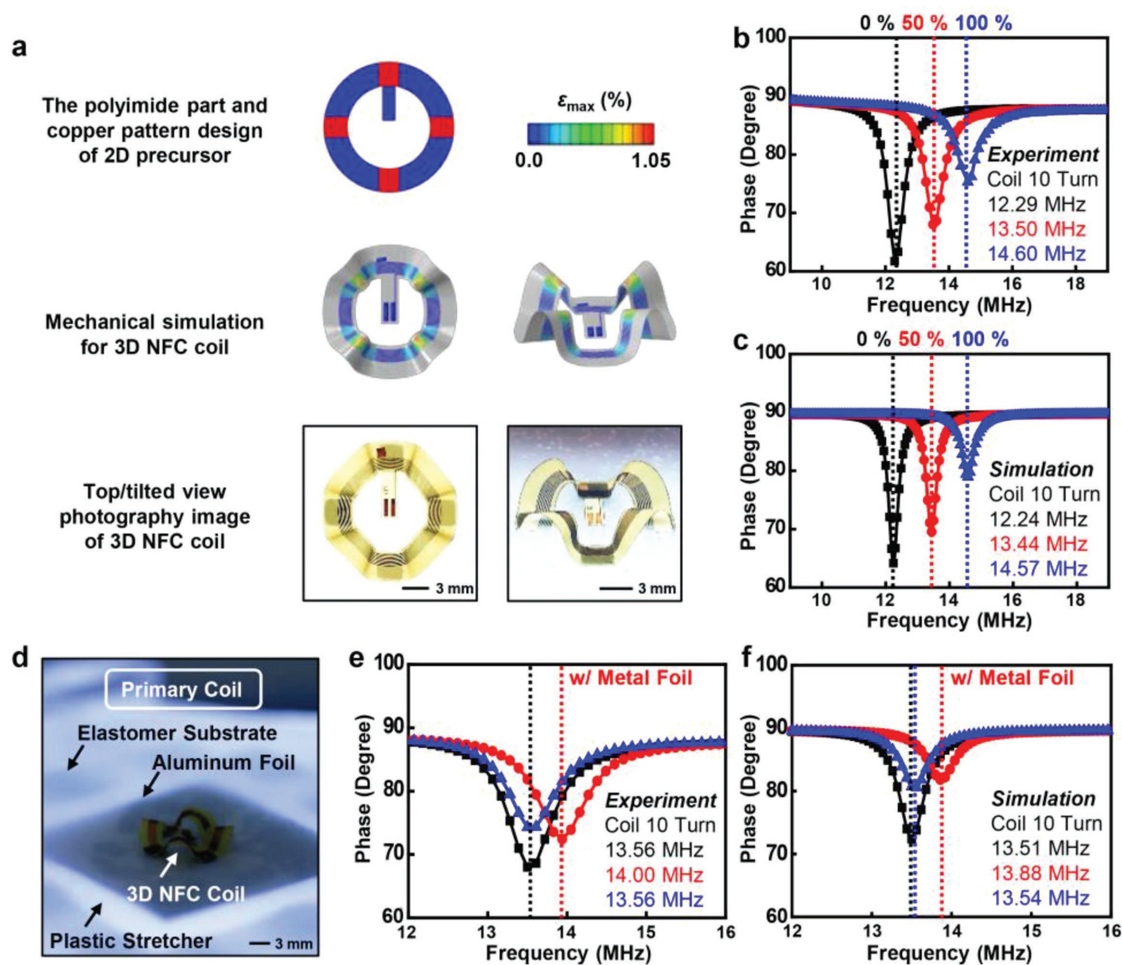

Figure 3. Design and operation of an adaptable, wireless 3D circuit system. a) Image of a 3D NFC antenna coil (metal thickness = 9 µm, line width/space = 70/75 µm, outer diameter = 15.5 mm, number of turns = 10) used in the experiment and mechanical simulation results after 3D assembly. The elastomer substrate has an initial prestrain of 100% biaxial. b,c) Graphs of phase response of the antenna determined experimentally and by EM simulation when the prestretched silicone elastomer is released by 0, 50, and 100%. The resonance frequencies change from 12.29 to 14.6 MHz. d) Image of the elastomer substrate (thickness ≈ 1.5 mm) loaded onto a plastic stretching stage with a piece of aluminum foil (thickness ≈ 25 µm) placed beneath the substrate. e,f) Experimental and EM simulation results showing shifts in the resonance frequency due to the aluminum foil, and recovery back to 13.56 MHz via deformations induced by stretching the elastomer.

dark (step 1), (ii) while exposed to ceiling lighting (step 2), (iii) while exposed to both ceiling lighting and a flashlight (step 3). Figure 2f presents measurements under room light conditions with a green laser incident at 45° in experiments described above as the silicone substrate is stretched and released. In the 2D and 3D shapes, the system shows negligible (stage 1) and strong (stage 2) responses, respectively. Such capabilities of reversible reconfiguration in shape might support interesting design opportunities in systems that embed automated mechanisms for actuation in soft robotics, for example.[46,47]

Similar strategies in mechanical tuning allow reversible adjustment of the resonance frequencies of antennas. **Figure 3**a shows images and mechanical simulation results for a magnetic loop antenna for NFC (metal thickness = 9 µm, line width/space = 70/75 µm, outer diameter = 15.5 mm, number of turns = 10) selectively bonded to a prestretched (50% biaxially) silicone elastomer. The coil (capacitor = 62 pF) has a resonance frequency of 13.56 MHz in a configuration with the prestrain released to 50%. Stretching/releasing allows for tuning the peak in the phase response (Figure 3b and Figure S4, Supporting Information) across a range from 12.29 to 14.6 MHz (released by 0 and 100%, respectively). Stretching/releasing the substrate transforms the resulting 3D device into different configurations, thus allowing for tunability in the peak. The dimensional changes can be captured with parameters such as the maximum out-of-plane displacement ($u_{3\text{-max}}$) and the aspect ratio defined as $u_{3\text{-max}}/l_{\text{in-plane}}$, where $l_{\text{in-plane}}$ denotes the maximum in-plane dimension of the device. As shown in Figure 3b and Figure S5 (Supporting Information), as the aspect ratio varies from 0 for the device in its 2D configuration to 0.37 for the device in its fully assembled stage, the peak of the phase response increases from 12.29 to 14.6 MHz.

These experimental results match those from electromagnetic (EM) simulation (Figure 3c). Such tuning can, for example, be exploited to compensate for changes in the dielectric environment. As summarized in Figure 3d, placing a piece of aluminum

 © 2018 WILEY-VCH Verlag GmbH & Co. KGaA, Weinheim

16163028, 2018, 48, Downloaded from https://onlinelibrary.wiley.com/doi/10.1002/adfm.201803149 by Sungkyunkwan University, Wiley Online Library on [14/04/2024]. See the Terms and Conditions (https://onlinelibrary.wiley.com/terms-and-conditions) on Wiley Online Library for rules of use; OA articles are governed by the applicable Creative Commons License

foil (thickness ≈ 25 μm) under the substrate (thickness ≈ 1.5 mm) shifts the resonance frequency of the coil to 14 MHz. Through appropriate stretching, the resonance can be turned back to the 13.56 MHz design point (Figure 3e), in this case with a strain of 72%, consistent with EM simulation (Figure 3f).

These procedures provide simple and low-cost means for mass production of 3D FPCBs with diverse configurations. Even a single 2D layout enables access to many different 3D geometries, selected by the locations and lengths of cuts, the bonding sites, and the values of prestrain. **Figure 4** presents a

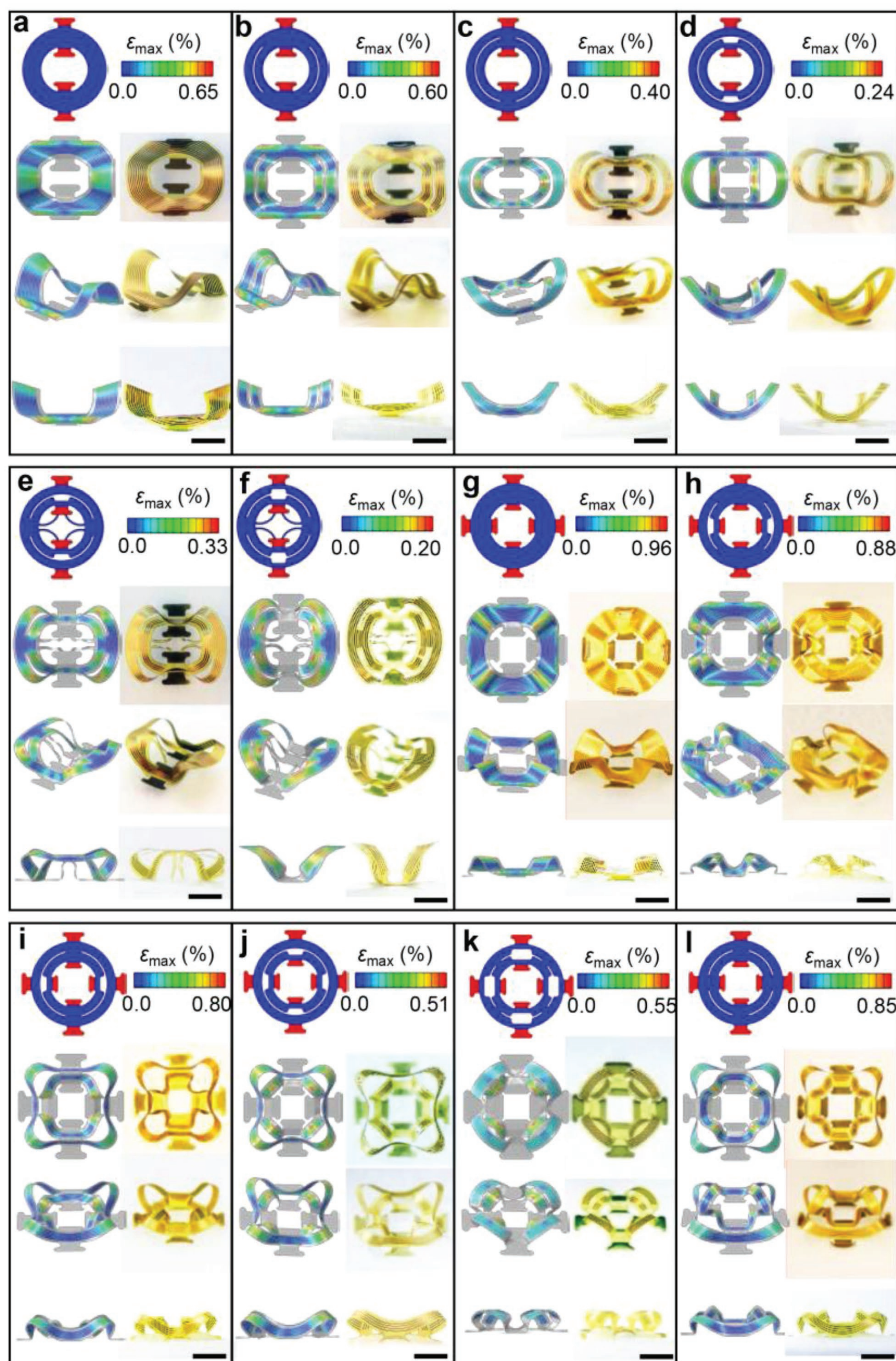

Figure 4. 12 different 3D circuit geometries realized by geometrical transformation of corresponding 2D FPCB platforms. a–l) The illustration at the top of each frame corresponds to a top view of the 2D precursor (red indicates bonding locations) and color scale bars for the strains; the other images show FEA predictions of the 3D structures (top, angled, and cross sectional) and corresponding optical images for designs that use uniaxial and biaxial prestrain. The color of the FEA results denotes the magnitude of maximum principal strain in copper layer (Scale bars: 4 mm).

 © 2018 WILEY-VCH Verlag GmbH & Co. KGaA, Weinheim

16163028, 2018, 48, Downloaded from https://onlinelibrary.wiley.com/doi/10.1002/adfm.201803149 by Sungkyunkwan University, Wiley Online Library on [14/04/2024]. See the Terms and Conditions (https://onlinelibrary.wiley.com/terms-and-conditions) on Wiley Online Library for rules of use; OA articles are governed by the applicable Creative Commons License

collection of examples with a commercial FPCB platform that consists of a bilayer of PI (12 µm) and copper (9 µm), transformed using either uniaxial (≈80%; Figure 4a–f) or biaxial (≈75%; Figure 4g–l) prestrain. Strains in the substrate can be achieved most simply by automated mechanical actuation, or by materials (e.g., shape memory polymers) that respond to changes in temperature or other parameters. The results presented here use a manually controlled stretcher. As shown in Figure 4, increasing the lengths of the cut reduces the strain in the copper, from 0.65 to 0.24% in Figure 4a–d (and from 0.96 to 0.51% in Figure 4g–j). Strain in the PI layer exhibits similar trends (Figure S6, Supporting Information). The location of cuts represents another important design parameter. As an example, Figure 4e highlights a design with cuts rotated 90° in the clockwise direction relative to those in Figure 4e. The resulting 3D geometries are qualitatively different, and cuts near the bonding sites significantly reduce the maximum strains in the constituent materials.

Patterns of cuts provide access to additional deformation modes. **Figure 5**a–d provides four representative examples, either with combinations of radial and circumferential cuts or with horseshoe-shaped cuts. These designs lead to enhanced rotational motions of the membrane components, as compared to those in Figure 4g–l. Variations in the overall shape of the 2D precursor lead to complex coil designs with additional twisting deformations, thereby expanding the 3D geometrical diversity of the assembled structures. Figure 5e–h provides four examples in this context, each with a specially designed coil pattern that fits the overall 2D precursor layout. In particular, the design in Figure 5f has potential as a platform for NFC systems with coils on four elevated circles. Here, the geometry of the coils remains nearly unchanged during tensile/compressive deformations of the substrate, for strain-insensitive electromagnetic performance. In all of the examples in Figures 4 and 5, 2D-to-3D assembly retains the symmetry of the 2D precursor, suggesting highly uniform and reproducible processes of transformation. FEA predictions agree well with the experimental results, in all cases (Figure S7, Supporting Information).

The 3D assembly process that yields the structures in Figures 4 and 5 occurs in a single-step fashion, applicable to

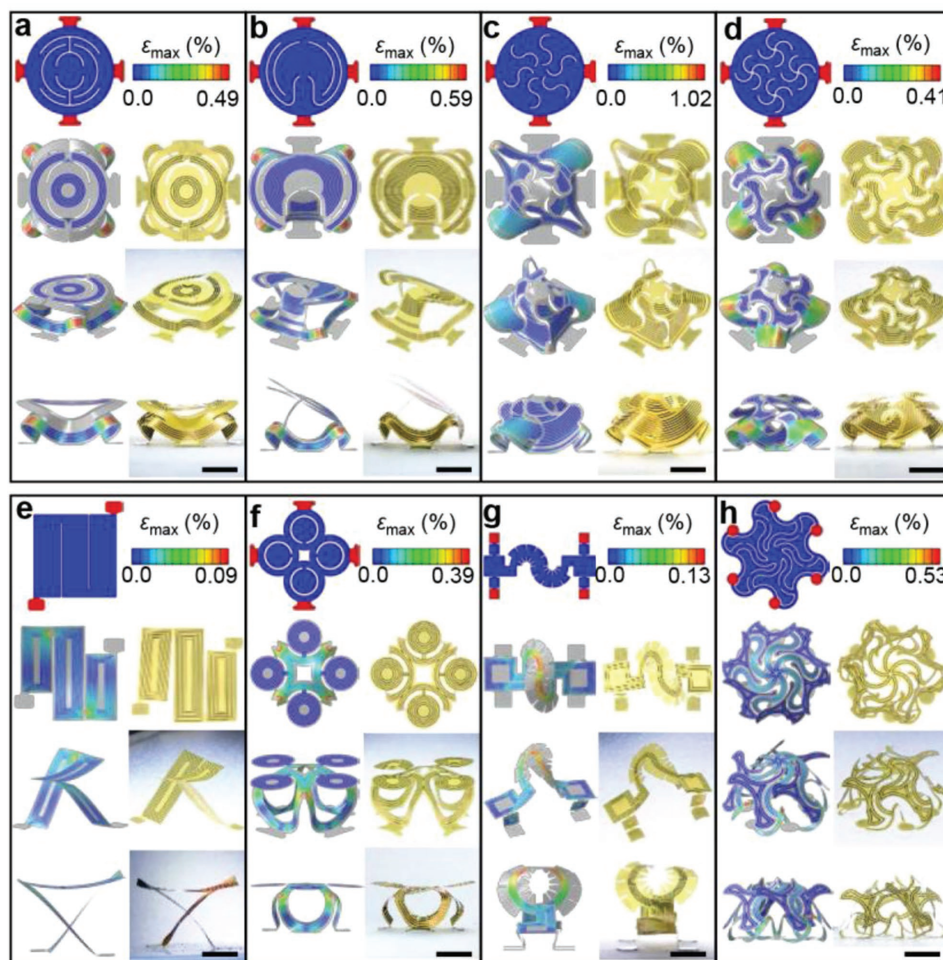

Figure 5. Eight different 3D circuit geometries realized by geometrical transformation of corresponding 2D FPCB platforms. a–h) The illustration at the top of each frame corresponds to a top view of the 2D precursor (red indicates bonding locations) and color scale bars for the strains; the other images show FEA predictions of the 3D structures (top, angled, and cross sectional) and corresponding optical images for designs that use uniaxial and biaxial prestrain. The color of the FEA results denotes the magnitude of maximum principal strain in copper layer (Scale bars: 4 mm).

16163028, 2018, 48, Downloaded from https://onlinelibrary.wiley.com/doi/10.1002/adfm.201803149 by Sungkyunkwan University, Wiley Online Library on [14/04/2024]. See the Terms and Conditions (https://onlinelibrary.wiley.com/terms-and-conditions) on Wiley Online Library for rules of use; OA articles are governed by the applicable Creative Commons License

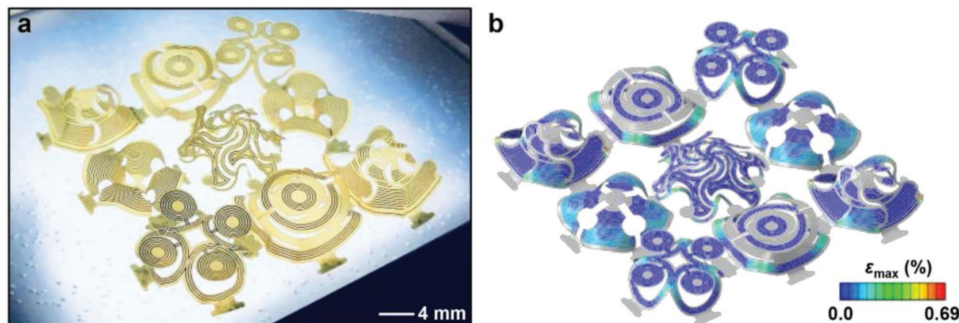

Figure 6. a) Optical image and b) FEA results for an array of 3D FPCB systems fabricated in a single-step, parallel assembly process.

arrays of isolated or interconnected 3D systems, over large areas. **Figure 6** shows an example that consists of a diverse collection of 3D FPCB architectures formed in a structured array, along with FEA simulations that agree with experimental results. The ability to operate in a parallel manner represents a distinct advantage in terms of throughput and cost. The basic strategy can, in fact, scale to areas limited only by the sizes of the elastomer substrates and the stages for creating and releasing the necessary prestrain. The various 3D geometries in Figures 4–6 simply show the ability to access a diversity of complex 3D circuit topologies. Such capabilities could provide routes to unusual functions, as directions for future work.

3. Conclusion

The results presented here demonstrate that processes of mechanical assembly can transform conventional 2D FPCBs, with or without surface mounted components, into 3D forms. The ability to reversibly change the shapes of these 3D constructs enables functional tuning, as illustrated in platforms that combine LEDs, PDs, microcontrollers, and NFC methods for energy harvesting and two-way data communication. Adjusting the 3D shapes modulates the electromagnetic operation, from optical sensing and radio frequency tuning. An attractive feature of these strategies is that they are naturally compatible with advanced circuit designs and chip-scale components, packaged or unpackaged, in conventional and various electronic, optoelectronic, and energy devices. Collectively, these features suggest new opportunities in circuit/system-level design applicable to 3D dynamic platforms,[48] biological systems,[49] and classes of sensors/actuators.[50]

4. Experimental Section

Fabrication of FPCB Systems: A metallized sheet of polyimide (9 µm thick copper and 12 µm thick polyimide, DOW chemical) served as the starting point for the fabrication process. Laminating this FPCB substrate onto a glass slide coated with poly(dimethylsiloxane) (PDMS; 10:1, Sylgard 184), with the polyimide side down, allowed patterning of the copper layer by photolithography (photoresist AZ 4620, spin-casting at 3500 rpm for 40 s, baking on a hot plate at 120 °C for 5 min, UV irradiance for 500 mJ cm^{-2}, development for ≈120 s with developer AZ 400K/deionized (DI) water solution of 1:3 volume ratio) and wet etching (CE-100 copper etchant, Transense, 3 min). Laser cutting removed selected regions of the resulting platform (LPKF ProtoLaser S4).

Process for 3D Assembly: Electron beam evaporation of Ti/SiO_2 (thickness ≈ 3/30 nm) through a metal shadow mask defined bonding sites on the exposed backside of the FPCB. A prestrained silicone substrate (Ecoflex, Smooth-On) activated by exposure to ultraviolet-induced ozone (UVO, 3 min) allowed chemical bonding to the FPCB upon contact and thermal annealing at 70 °C for 3 min. Releasing the prestrain initiated the process for geometrical transformation of the 2D FPCB into a 3D configuration.

Mechanics Simulations: FEA used commercial software ABAQUS with conventional static analysis to simulate the compressive buckling processes. Eight-node 3D solid elements (C3D8R) and four-node shell elements (S4R) were used to model the silicone substrate and 2D precursors, respectively. Convergence of mesh sizes was tested to ensure computational accuracy. The critical buckling strains and corresponding buckling modes determined from linear buckling analyses were implemented as initial imperfections in the postbuckling calculations to obtain the deformed configurations and strain distributions of the 3D FPCB structures. The elastic modulus (E) and Poisson's ratio (ν) are $E_{substrate}$ = 60 kPa and $\nu_{substrate}$ = 0.49 for substrate; E_{Cu} = 119 GPa and ν_{Cu} = 0.34 for copper; and E_{PI} = 2.5 GPa and ν_{PI} = 0.34 for PI.

Electromagnetic Simulations: The finite element method was adopted in electromagnetic simulations to calculate the impedance, Q factor, and phase angle of the 3D NFC devices. The simulations were conducted using the commercial software ANSYS HFSS, in which tetrahedron elements with adaptive meshing convergence were used. The 3D configurations of the devices determined by the mechanics simulations were imported to the software ANSYS HFSS, and then thickened to the desired thickness to complete the preprocessing of the geometric models. The PI layers in the devices were ignored due to their negligible influence on the simulation results. The relative permittivity (ε_r), relative permeability (μ_r), and conductivity (σ) are ε_{r_Cu} = 1, μ_{r_Cu} = 0.999991, and $\sigma_{Cu} = 5.8 \times 10^7$ S m^{-1} for copper; $\varepsilon_{r_substrate}$ = 2.55, $\mu_{r_substrate}$ = 1, and $\sigma_{substrate} = 2.5 \times 10^{-14}$ S m^{-1} for substrate.

Supporting Information

Supporting Information is available from the Wiley Online Library or from the author.

Acknowledgements

B.H.K., F.L., Y.Y., and H.J. contributed equally to this work. Z.X. acknowledges the support from National Natural Science Foundation of China (Grant No. 11402134). Y.H. acknowledges the support from NSF (Grant Nos. 1400169, 1534120, and 1635443). Y.Z. acknowledges support from the National Natural Science Foundation of China (Nos. 11672152 and 11722217) and the Thousand Young Talents Program of China and the Tsinghua National Laboratory for Information Science and Technology.

 © 2018 WILEY-VCH Verlag GmbH & Co. KGaA, Weinheim

Conflict of Interest

The authors declare no conflict of interest.

Keywords

3D electronic devices, kirigami, mechanical buckling, near-field communication, origami

Received: May 7, 2018
Revised: August 15, 2018
Published online: September 25, 2018

[1] A. Balasubramanian, C. J. Bettinger, *Adv. Eng. Mater.* **2015**, *17*, 1287.
[2] C. J. Bettinger, E. J. Weinberg, K. M. Kulig, J. P. Vacanti, Y. Wang, J. T. Borenstein, R. Langer, *Adv. Mater.* **2006**, *18*, 165.
[3] S. A. Morin, Y. Shevchenko, J. Lessing, S. W. Kwok, R. F. Shepherd, A. A. Stokes, G. M. Whitesides, *Adv. Mater.* **2014**, *26*, 5991.
[4] J. N. H. Shepherd, S. T. Parker, R. F. Shepherd, M. U. Gillette, J. A. Lewis, R. G. Nuzzo, *Adv. Funct. Mater.* **2011**, *21*, 47.
[5] J. Odent, T. J. Wallin, W. Pan, K. Kruemplestaedter, R. F. Shepherd, E. P. Giannelis, *Adv. Funct. Mater.* **2017**, *27*, 1701807.
[6] Y.-L. Sun, Q. Li, S.-M. Sun, J.-C. Huang, B.-Y. Zheng, Q.-D. Chen, Z.-Z. Shao, H.-B. Sun, *Nat. Commun.* **2015**, *6*, 8612.
[7] B. Y. Ahn, E. B. Duoss, M. J. Motala, X. Guo, S.-I. Park, Y. Xiong, J. Yoon, R. G. Nuzzo, J. A. Rogers, J. A. Lewis, *Science* **2009**, *323*, 1590.
[8] C. S. O'Bryan, T. Bhattacharjee, S. Hart, C. P. Kabb, K. D. Schulze, I. Chilakala, B. S. Sumerlin, W. G. Sawyer, T. E. Angelini, *Sci. Adv.* **2017**, *3*, e1602800.
[9] C. Zhu, T. Y.-J. Han, E. B. Duoss, A. M. Golobic, J. D. Kuntz, C. M. Spadaccini, M. A. Worsley, *Nat. Commun.* **2015**, *6*, 6962.
[10] X. Tian, J. Jin, S. Yuan, C. K. Chua, S. B. Tor, K. Zhou, *Adv. Energy Mater.* **2017**, *7*, 1700127.
[11] A. D. Valentine, T. A. Busbee, J. W. Boley, J. R. Raney, A. Chortos, A. Kotikian, J. D. Berrigan, M. F. Durstock, J. A. Lewis, *Adv. Mater.* **2017**, *29*, 1703817.
[12] S. Huang, L. Zhang, X. Lu, L. Liu, L. Liu, X. Sun, Y. Yin, S. Oswald, Z. Zou, F. Ding, O. G. Schmidt, *ACS Nano* **2016**, *11*, 821.
[13] Y. L. Kong, I. A. Tamargo, H. Kim, B. N. Johnson, M. K. Gupta, T.-W. Koh, H.-A. Chin, D. A. Steingart, B. P. Rand, M. C. McAlpine, *Nano Lett.* **2014**, *14*, 7017.
[14] B. H. Kim, Y. Choi, J. Y. Kim, H. Shin, S. Kim, S.-W. Son, S. O. Kim, P. Kim, *Adv. Mater.* **2014**, *26*, 4665.
[15] J. U. Lind, T. A. Busbee, A. D. Valentine, F. S. Pasqualini, H. Yuan, M. Yadid, S.-J. Park, A. Kotikian, A. P. Nesmith, P. H. Campbell, J. J. Vlassak, J. A. Lewis, K. K. Parker, *Nat. Mater.* **2017**, *16*, 303.
[16] J. T. B. Overvelde, T. A. de Jong, Y. Shevchenko, S. A. Becerra, G. M. Whitesides, J. C. Weaver, C. Hoberman, K. Bertoldi, *Nat. Commun.* **2016**, *7*, 10929.
[17] Z. Song, T. Ma, R. Tang, Q. Cheng, X. Wang, D. Krishnaraju, R. Panat, C. K. Chan, H. Yu, H. Jiang, *Nat. Commun.* **2014**, *5*, 3140.
[18] S. Waitukaitis, R. Menaut, B. G. Chen, M. van Hecke, *Phys. Rev. Lett.* **2015**, *114*, 055503.
[19] J. L. Silverberg, A. A. Evans, L. McLeod, R. C. Hayward, T. Hull, C. D. Santangelo, I. Cohen, *Science* **2014**, *345*, 647.
[20] L. H. Dudte, E. Vouga, T. Tachi, L. Mahadevan, *Nat. Mater.* **2016**, *15*, 583.
[21] J. Rogers, Y. Huang, O. G. Schmidt, D. H. Gracias, *MRS Bull.* **2016**, *41*, 123.
[22] H. Hu, C. Huang, X. H. Liu, K. J. Hsia, *Extreme Mech. Lett.* **2016**, *8*, 107.
[23] W. Huang, S. Koric, X. Yu, K. J. Hsia, X. Li, *Nano Lett.* **2014**, *14*, 6293.
[24] J. H. Pikul, S. Li, H. Bai, R. T. Hanlon, I. Cohen, R. F. Shepherd, *Science* **2017**, *358*, 210.
[25] S. H. Tawfick, J. Bico, S. Barcelo, *MRS Bull.* **2016**, *41*, 108.
[26] A. Tocchio, N. G. Durmus, K. Sridhar, V. Mani, B. Coskun, R. E. Assal, U. Demirci, *Adv. Mater.* **2017**, *30*, 1705034.
[27] S. Pautot, C. Wyart, E. Y. Isacoff, *Nat. Methods* **2008**, *5*, 735.
[28] M. Humood, Y. Shi, M. Han, J. Lefebvre, Z. Yan, M. Pharr, Y. Zhang, Y. Huang, J. A. Rogers, A. A. Polycarpou, *Small* **2018**, *14*, 1703852.
[29] S. Xu, Z. Yan, K.-I. Jang, W. Huang, H. Fu, J. Kim, Z. Wei, M. Flavin, J. McCracken, R. Wang, A. Badea, Y. Liu, D. Xiao, G. Zhou, J. Lee, H. U. Chung, H. Cheng, W. Ren, A. Banks, X. Li, U. Paik, R. G. Nuzzo, Y. Huang, Y. Zhang, J. A. Rogers, *Science* **2015**, *347*, 154.
[30] Y. Zhang, F. Zhang, Z. Yan, Q. Ma, X. Li, Y. Huang, J. A. Rogers, *Nat. Rev. Mater.* **2017**, *2*, 17019.
[31] Y. Zhang, Z. Yan, K. Nan, D. Xiao, Y. Liu, H. Luan, H. Fu, X. Wang, Q. Yang, J. Wang, W. Ren, H. Si, F. Liu, L. Yang, H. Li, J. Wang, X. Guo, H. Luo, L. Wang, Y. Huang, J. A. Rogers, *Proc. Natl. Acad. Sci. USA* **2015**, *112*, 11757.
[32] W. C. Leong, M. Z. Abdullah, C. Y. Khor, *Microelectron. Reliab.* **2012**, *52*, 744.
[33] C. Han, C. Zhang, W. Tang, X. Li, Z. L. Wang, *Nano Res.* **2015**, *8*, 722.
[34] Z. Yan, F. Zhang, F. Liu, M. Han, D. Ou, Y. Liu, Q. Lin, X. Guo, H. Fu, Z. Xie, M. Gao, Y. Huang, J. Kim, Y. Qiu, K. Nan, J. Kim, P. Gutruf, H. Luo, A. Zhao, K.-C. Hwang, Y. Huang, Y. Zhang, J. A. Rogers, *Sci. Adv.* **2016**, *2*, e1601014.
[35] Y. Sun, W. M. Choi, H. Jiang, Y. Y. Huang, J. A. Rogers, *Nat. Nanotechnol.* **2006**, *1*, 201.
[36] Z. Yan, F. Zhang, J. Wang, F. Liu, X. Guo, K. Nan, Q. Lin, M. Gao, D. Xiao, Y. Shi, Y. Qiu, H. Luan, J. H. Kim, Y. Wang, H. Luo, M. Han, Y. Huang, Y. Zhang, J. A. Rogers, *Adv. Funct. Mater.* **2016**, *26*, 2629.
[37] K.-I. Jang, K. Li, H. U. Chung, S. Xu, H. N. Jung, Y. Yang, J. W. Kwak, H. H. Jung, J. Song, C. Yang, A. Wang, Z. Liu, J. Y. Lee, B. H. Kim, J.-H. Kim, J. Lee, Y. Yu, B. J. Kim, H. Jang, K. J. Yu, J. Kim, J. W. Lee, J.-W. Jeong, Y. M. Song, Y. Huang, Y. Zhang, J. A. Rogers, *Nat. Commun.* **2017**, *8*, 15894.
[38] K.-I. Jang, H. U. Chung, S. Xu, C. H. Lee, H. Luan, J. Jeong, H. Cheng, G.-T. Kim, S. Y. Han, J. W. Lee, J. Kim, M. Cho, F. Miao, Y. Yang, H. N. Jung, M. Flavin, H. Liu, G. W. Kong, K. J. Yu, S. I. Rhee, J. Chung, B. Kim, J. W. Kwak, M. H. Yun, J. Y. Kim, Y. M. Song, U. Paik, Y. Zhang, Y. Huang, J. A. Rogers, *Nat. Commun.* **2015**, *6*, 6566.
[39] Dupont Kapton Summary of Properties, http://www.dupont.com/content/dam/dupont/products-and-services/membranes-and-films/polyimde-films/documents/DEC-Kapton-summary-of-properties.pdf, (accessed: January 2018).
[40] Q. Wang, M. Tahir, J. Zang, X. Zhao, *Adv. Mater.* **2012**, *24*, 1947.
[41] M. Kubo, X. Li, C. Kim, M. Hashimoto, B. J. Wiley, D. Ham, G. M. Whitesides, *Adv. Mater.* **2010**, *22*, 2749.
[42] S. Xu, Y. Zhang, J. Cho, J. Lee, X. Huang, L. Jia, J. A. Fan, Y. Su, J. Su, H. Zhang, H. Cheng, B. Lu, C. Yu, C. Chuang, T.-I. Kim, T. Song, K. Shigeta, S. Kang, C. Dagdeviren, I. Petrov, P. V. Braun, Y. Huang, U. Paik, J. A. Rogers, *Nat. Commun.* **2013**, *4*, 1543.
[43] H. Fu, K. Nan, W. Bai, W. Huang, K. Bai, L. Lu, C. Zhou, Y. Liu, F. Liu, J. Wang, M. Han, Z. Yan, H. Luan, Y. Zhang, Y. Zhang, J. Zhao, X. Cheng, M. Li, J. W. Lee, Y. Liu, D. Fang, X. Li, Y. Huang, Y. Zhang, J. A. Rogers, *Nat. Mater.* **2018**, *17*, 268.
[44] Y. Zhang, Z. Yan, K. Nan, D. Xiao, Y. Liu, H. Luan, H. Fu, X. Wang, Q. Yang, J. Wang, W. Ren, H. Si, F. Liu, L. Yang, H. Li, J. Wang, X. Guo, H. Luo, L. Wang, Y. Huang, J. A. Rogers, *Proc. Natl. Acad. Sci. USA* **2015**, *112*, 11757.
[45] S. Han, J. Kim, S. M. Won, Y. Ma, D. Kang, Z. Xie, K.-T. Lee, H. U. Chung, A. Banks, S. Min, S. Y. Heo, C. R. Davies, J. W. Lee,

 © 2018 WILEY-VCH Verlag GmbH & Co. KGaA, Weinheim

16163028, 2018, 48, Downloaded from https://onlinelibrary.wiley.com/doi/10.1002/adfm.201803149 by Sungkyunkwan University, Wiley Online Library on [14/04/2024]. See the Terms and Conditions (https://onlinelibrary.wiley.com/terms-and-conditions) on Wiley Online Library for rules of use; OA articles are governed by the applicable Creative Commons License

C.-H. Lee, B. H. Kim, K. Li, Y. Zhou, C. Wei, X. Feng, Y. Huang, J. A. Rogers, *Sci. Transl. Med.* **2018**, *10*, eaan4950.
[46] R. F. Shepherd, F. Ilievski, W. Choi, S. A. Morin, A. A. Stokes, A. D. Mazzeo, X. Chen, M. Wang, G. M. Whitesides, *Proc. Natl. Acad. Sci. USA* **2011**, *108*, 20400.
[47] C. Huang, D. Quinn, S. Suresh, K. J. Hsia, *Proc. Natl. Acad. Sci. USA* **2018**, *115*, 70.
[48] X. Ning, H. Wang, X. Yu, J. A. N. T. Soares, Z. Yan, K. Nan, G. Velarde, Y. Xue, R. Sun, Q. Dong, H. Luan, C. M. Lee, A. Chempakasseril, M. Han, Y. Wang, L. Li, Y. Huang, Y. Zhang, J. A. Rogers, *Adv. Funct. Mater.* **2017**, *27*, 1605914.
[49] B. G. Compton, J. A. Lewis, *Adv. Mater.* **2014**, *26*, 5930.
[50] J. Y. Kim, J. Lim, H. M. Jin, B. H. Kim, S.-J. Jeong, D. S. Choi, D. J. Li, S. O. Kim, *Adv. Mater.* **2016**, *28*, 1591.

© 2018 WILEY-VCH Verlag GmbH & Co. KGaA, Weinheim

16163028, 2018, 48, Downloaded from https://onlinelibrary.wiley.com/doi/10.1002/adfm.201803149 by Sungkyunkwan University, Wiley Online Library on [14/04/2024]. See the Terms and Conditions (https://onlinelibrary.wiley.com/terms-and-conditions) on Wiley Online Library for rules of use; OA articles are governed by the applicable Creative Commons License